ACS OMEGA

Open Access

http://pubs.acs.org/journal/acsodf

Article

Valorizing Biopolyester Suberin: Modification of Cellulose Nanocrystals and Performance Assessment in 3D-Printed Biobased Acrylates

Beate Beatrise Bruvere, Anda Gromova, Maksims Jurinovs, Oskars Platnieks, Jānis Rižikovs, Aigars Pāže, Daniela Godiņa, Inese Mieriņa, Ivo Heinmaa, Krisjanis Smits, Vitālijs Rjabovs, and Sergejs Gaidukovs*

Cite This: *ACS Omega* 2024, 9, 42786−42798

Read Online

ACCESS | Metrics & More | Article Recommendations | Supporting Information

ABSTRACT: Suberin, a common biomass processing waste, is a complex biopolymer and a promising source for the biorefinery of chemicals. Six different approaches for the extraction of birch outer bark suberin fatty acids (SFAs) were explored, and their application in grafting the surface of cellulose nanocrystals (CNCs) was investigated. Successful CNC functionalization was controlled with FTIR and NMR analyses. In-depth research allowed us to evaluate the interface of the nanocellulose and polymer matrix. Three structurally distinct SFA-grafted CNCs were integrated into a vegetable oil-based acrylate resin in an ultralow concentration of 0.1 wt %. Five biobased acrylic resin formulations were prepared: without reinforcement, with CNC, and with three distinct SFA-grafted CNCs. Vat photopolymerization (VP) 3D printing was utilized for sample preparation. The effects of grafted CNC components on 3D-printed samples' thermal stability, thermomechanical properties, and wettability were evaluated in detail. CNC functionalization enhanced the interface with the polymer matrix, yielding up to a 2-fold increase in elongation and up to a 2.5-fold increase in strength in tensile and flexural tests compared to the polymeric matrix. The CNC-SFA-modified filler demonstrated performance comparable to, or even better than, petroleum-based chemical modification routes found in the existing literature. This study highlights a promising approach for green functionalization of CNCs and verifies its use in interface enhancement using a biobased acrylate matrix.

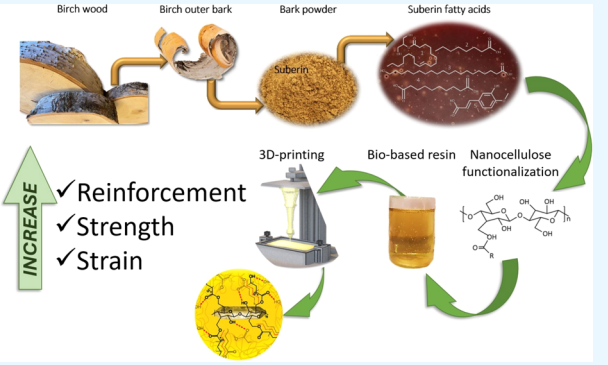

INTRODUCTION

A global shift toward environmentally conscious material usage has recently accentuated the intersection of bioderived material research and additive manufacturing technology.[1,2] The need to avoid the environmental hazards posed by petroleum-derived and synthetic polymers, particularly in terms of pollution reduction, is driving the green revolution.[1] 3D printing, especially vat photopolymerization (VP), recognized for its capacity to generate objects with exquisite precision and surface quality, has permeated various industries owing to its ability to materialize complex designs.[3] VP predominantly utilizes petroleum-based resins, but with the growing interest in sustainable practices, the exploration of biobased resins, such as those derived from vegetable oils, has been propelled to the forefront.[4] Despite presenting a sustainable avenue, bioacrylate resins have encountered challenges in matching the mechanical properties of their synthetic counterparts, necessitating further innovation and research in this domain.[5]

A very promising route to enhance the properties of polymeric structures is the use of compatible fillers, which can reinforce the structure and improve the mechanical properties. Derived from the most abundant natural polymer, cellulose nanocrystals (CNC) manifest substantial applicative promise across diverse industries.[6] Surface modification of CNC not only confers specialized functionalities but also enhances interfacial compatibility with various materials and augments dispersion within distinct polymer matrices. As a result, it facilitates their aptitude to cater to tailored applications across a multitude of industries.[7] Consequently, the strategic alteration of CNC surfaces emerges as a pivotal approach to harnessing their potential. Many attempts have been reported to improve CNC and polymer matrix interfaces via CNC surface modifications.[8−10] For example, Feng et al. coated CNC with lignin and achieved increased thermal stability and storage modulus.[8] Functionalization of CNC with methacrylate and methyl methacrylate showed better dispersibility and

Received: May 9, 2024
Revised: September 5, 2024
Accepted: September 25, 2024
Published: October 9, 2024

increased glass transition.[10] In our previous investigations with vegetable oil-based composites, functionalization of CNC with isocyanate resulted in up to a 30% increase in interfacial adhesion and 2.4 times higher tensile strength.[11] Nanocellulose has also been acrylated to improve compatibility with the acrylate polymer matrix.[12] The CNC functionalization in the literature indicates impressive results; however, these modifications have often yielded reduced biobased content and sustainability.[13,14] Therefore, more research should concentrate on finding sustainable CNC surface functionalization paths with biobased materials.

Promising sources of biobased chemicals are various forestry resources, which do not directly compete for valuable agricultural lands. Suberin, a renewable biopolyester, consists of polyfunctional long-chain fatty acids and glycerol, featuring both linear alkyl chains and aromatic monomers interconnected by acylglycerol or linear aliphatic esters.[15] With proven adhesive and hydrophobic properties, this biopolymer acts as a vital protective barrier against external environmental factors and regulates water movement.[16−19] Notably, birch, prevalent in Northern Europe, contains a suberin concentration of 20−45% within its outer bark, presenting a substantially underutilized material resource currently being relegated to energy production via biomass incineration.[20] The outer bark of birch logs makes up approximately 2.0−3.4% of their total composition.[21] For example, a birch Kraft pulp mill, with an annual production of 400,000 tons/year, and a plywood factory, with an annual production of 252,000 m^3/year, generate approximately 28,000 and 16,000 tons of outer bark, respectively.[21] Suberin fatty acids (SFA), derived through suberin hydrolysis, are prominent monomers with polar and nonpolar adhesion and hydrophobicity properties. When SFAs are integrated into polymer systems, they enhance mechanical, thermal, and barrier properties while conferring resistance to moisture and chemicals.[16,22] Qasim et al. developed biogenic and multifunctional active food coatings and packaging materials that exhibited UV shielding and antimicrobial properties.[23] These materials were structured from an aqueous dispersion of suberin and stabilized using amphiphilic cellulose nanofibers. Shulga et al. utilized suberin acids as lubricants in the formulation of recycled polypropylene/polylactic acid composites filled with alkali-treated milled birch shaving microparticles.[24] At optimal content levels, these lubricants enhanced the processing of the composite, improved mechanical properties, and decreased the wettability of the composite. Depending on the depolymerization conditions, SFAs have different chemical properties and application possibilities.[22] SFA could be used for cellulose surface functionalization[25] and aid in reducing the hydrophilicity and hence improving the cellulose-polymer interface. Therefore, leveraging the multifunctionality of SFA paves the way for advancing biobased composites, endorsing material innovation and sustainability in polymer applications.

The primary objective of this work was to improve the compatibility between the filler and matrix interfaces by using chemicals produced through the biorefinery process in the functionalization method. The present study explored a promising CNC functionalization route using bioderived SFAs with different acid group contents. Six different suberin extraction procedures were applied to obtain SFA. Employing the degree of hydroxyl group substitution as a criterion for discerning CNC-SFA variations, three distinct functionalized CNC-SFA fillers were chosen. The analysis was based on their performance within biobased vegetable oil-acrylate resins, which were subsequently 3D-printed utilizing the VP technique. This research outlines the innovative use of SFA in functionalizing CNC for advanced applications in 3D printing resins without significant loss of biobased content.

MATERIALS AND METHODS

Materials. Acrylated epoxidized soybean oil (AESO) (contains 3500−4500 ppm monomethyl ether hydroquinone as an inhibitor, viscosity 18,000−32,000 cps.); reactive diluents: trimethylolpropane triacrylate (TMPTA) (purity of >70.00%, contains 500−750 ppm monomethyl ether hydroquinone as an inhibitor) and 1,6-hexanediol diacrylate-technical grade (HDDA) (purity 77.5%); photoinitiator (PI): diphenyl(2,4,6-trimethyl-benzoyl) phosphine oxide (TPO); high purity (≥99.0%) chemicals−iron(II) sulfate heptahydrate, hydrogen peroxide (30%), acetone, ethanol, maleic anhydride (MAH), cerium ammonium nitrate (CAN) were purchased from Sigma-Aldrich (Steinheim, Germany). Potassium hydroxide (KOH) (Reag. Ph Eur, 85.0−100.5%) was provided by VWR International (Leuven, Belgium). Nitric acid (HNO_3) (≥65%) was obtained from Honeywell (Seelze, Germany). All received chemicals were used as is, except in instances where specific processing was stated. Dry ethanol was made with molecular sieves. Cellulose nanocrystals (CNC) were obtained by processing *Santhica* 27 variety hemp stalks (sourced locally in Latvia). Deionized water was filtered in the lab (<0.05 μS cm^1). Suberin fatty acids (SFA) were extracted from birch outer bark industrial waste provided by the JSC Latvijas Finieris plywood factory (Riga, Latvia).

Raw Material—Birch Outer Bark Processing. Birch outer bark from the plywood factory JSC Latvijas Finieris was selected as a representative industrial waste. Bark samples were dried at room temperature (to a moisture content of 4−5%) and milled in an SM 100 cutting mill (Retsch GmbH, Haan, Germany) through a sieve with a 4 mm aperture. Milled bark was fractionated by sieving with an AS 200 Basic vibratory sieve shaker (Retsch GmbH, Haan, Germany); a fraction of 1−3.15 mm was collected. Fractionated birch outer bark was extracted with ethanol twice, as described by Godiņa et al.[26] The referenced article also provides a full list of the extracted compounds. After extraction, the outer bark solid residue, with a moisture content of 5−6%, was used as feedstock for depolymerization. The extraction process removed other bark fractions, such as triterpenes like betulin and lupeol, for various applications (cosmetics, food supplements, or medicine) and enhanced the purity and yield of suberin in the birch outer bark.

Sample Preparation. *Suberin Fatty Acid Extraction.* The following procedure describes extraction approach variations and the resulting six SFA products (SL, SL1, SM, SM1, SH, and SH1). Six types of SFA were abbreviated according to acid group content: high (SH, SH1), medium (SM, SM1), and low (SL, SL1). The comparison of SFA extraction conditions is provided in Table S1. About 80 g of dry processed birch outer bark was depolymerized in 800 mL of KOH at 0.30 mol (SM, SM1, and SL1), 0.65 mol (SH), and 1.00 mol (SL and SH1) ethanol−water solution (90% w/w) for 30 min (SM, SL, SH1, and SM1), 60 min (SH), and 90 min (SL1) at 50 °C (SM, SL, and SL1), and 80 °C (SH, SH1, and SM1). After depolymerization, the solution was cooled down to 30 °C and filtered through the 100 μm nonwoven polyamide fabric. The filtrate was evaporated until 70 vol % of the ethanol−

https://doi.org/10.1021/acsomega.4c04419
ACS Omega 2024, 9, 42786−42798

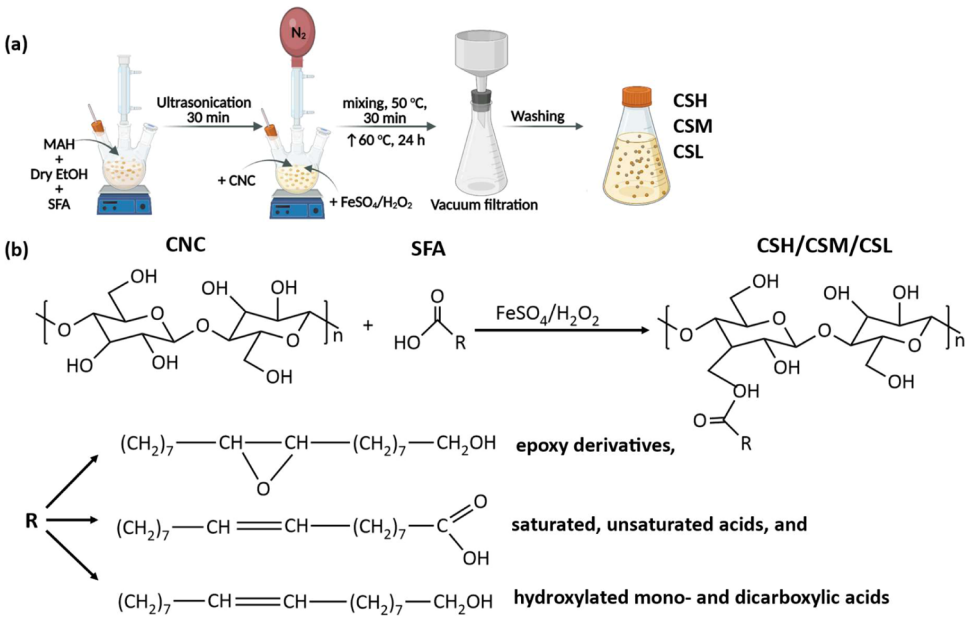

Figure 1. CNC functionalization with SFA: setup (a) and reaction scheme (b).

water solvent was recovered, followed by further dilution with 800 mL of water. The obtained suspension was acidified with HNO_3 to pH 1.0 (SH, SM, and SH1) and pH 6.0 (SL, SM1, and SL1) and filtered. The obtained slurry was rinsed with 800 mL of deionized water, followed by another filtration and drying at 50 °C for each sample. Gas chromatography−mass spectrometry (GC-MS) analysis of the SFA samples is described in the Supporting Information, and the results are summarized in Table S2.

Nanocellulose Preparation. The hemp stalks underwent a two-stage grinding process, initially being processed in a Retsch SM300 cutting mill equipped with 4.00 mm and 0.25 mm sieves for each pass. This was followed by an additional grinding step in a Retsch ZM200 mill fitted with a 0.12 mm sieve. The micronized hemp powder was then treated with a 10% sodium hydroxide (NaOH) water solution in a 1:8 ratio and heated at 80 °C for 3 h. Afterward, the NaOH solution was replaced with a fresh one and left overnight at room temperature (20 °C). The produced pulp was filtered and washed with deionized water until it reached a neutral pH. The wet mass was mixed with a 20% hydrochloric acid water solution in a 1:8 ratio (dry cellulose weight) and heated at 80 °C for 2 h. Subsequently, the processed cellulose was filtered and washed to a neutral pH. The cellulose was dried and mixed with water to produce a suspension with a concentration of 1 wt % and was then processed using an LM 20 Microfluidizer (USA) with a chamber H210Z (200 μm) and a pressure setting of 30,000 psi. Five passes through the microfluidizer were performed to produce cellulose nanocrystals (CNC).

CNC Functionalization with SFA. The reaction was conducted following a method outlined in the literature.[27] Reaction setup and scheme is shown in Figure 1. An aqueous suspension of CNC (0.5 g dry CNC weight) was solvent exchanged with an ethanol suspension and finally with a dry ethanol suspension. This solvent exchange process was achieved through centrifugation (using a 20 mL tube) and redispersion in an ultrasonic bath, employing five cycles (30 min at 9000 rpm). SFA (2.92 g) was dissolved in 50 mL of dry ethanol and mixed with an equal weight of 2.92 g of MAH. The CNC suspension was then combined with the dissolved SFA and stirred continuously for 30 min at 50 °C under an inert (N_2) atmosphere. Subsequently, a catalyst solution of $FeSO_4$ dissolved in H_2O_2 was gradually added (0.07 g $FeSO_4$ and 7 mL H_2O_2). The reaction mixture was left to stir continuously for 24 h at 50 °C. The final product was separated from the suspension using a Buchner funnel and washed with ethanol and water. This procedure was repeated six times to produce modified CNC fillers, abbreviated as CSL, CSL1, CSM, CSM1, CSH, and CSH1.

Preparation of the Resins. Monomers were mixed with a photoinitiator TPO dissolved in acetone, then AESO was added. The mixture was stirred mechanically for 1 h. The resin composition was formulated with 65/30/5 wt % of AESO, HDDA, and TMPTA. A 3:100 TPO/resin ratio was used for photoactive composition. In the final step, a CNC dispersion of acetone was added to the resin using a high-shear mixer for 5 min at 9000 rpm. Then, the resin was put in a vacuum chamber at 1000 mbar for 2 h to get rid of any extra air and leftover acetone. The resins were stored in a dark place to keep them from curing. Using this method, both plain resin and composite resins with four types of fillers (CNC, CSH, CSM, and CSL) were made. The nanocellulose filler concentration in the resin was fixed at 0.1 wt %. It was observed that the remaining resin (left over after sample printing) did not show any signs of sedimentation over the course of the month.

3D Printing of the Samples. Samples were printed with an Original Prusa SL1 3D printer (PRUSA research, Czech Republic), which uses a 5.5" LCD with 25 W LED power input and a UV wavelength of 405 nm. Two types of samples were printed for a flexural (80 × 10 × 4 mm) (ISO-178) test and tensile test (75 × 10 × 2 mm) (ISO-527 1BA). Layer height was set to 0.05 mm; for the first 10 layers, the exposure time was 35 s for proper sample adhesion to the printing platform. The following layers were printed with an exposure time of 15 s. After printing, the samples were washed with isopropanol to remove any leftover resin from the surface. Then, the printed samples were dried for 5 min and postcured for 3 min in an Original Prusa Curing and Washing Machine (UV wavelength

https://doi.org/10.1021/acsomega.4c04419
ACS Omega 2024, 9, 42786−42798

of 405 nm, 20 °C). Five printed sample compositions were characterized and consisted of a reference sample without filler (p0%), a sample with unmodified CNC filler (pCNC), and three with SFA-modified CNC filler (pCSH, pCSM, and pCSL). The abbreviations relate to the content of acid groups in the SFA (further discussed in the Results section).

Characterization/Methods. *Acid Number Determination.* To about 0.2 g of the sample, 5 mL of DMSO was added and stirred for 1 h. Afterward, 20 mL of i-PrOH and 5 mL of water were added, and the solution was titrated with a 0.1 M KOH solution. Two replicate experiments were performed for each sample. The acid number was calculated according to eq 1:

$$\text{acid number} = \frac{V_{\text{analyte}} \times C_{\text{KOH}} \times M_{\text{KOH}}}{m} \quad (1)$$

where V_{analyte} is the volume of the titrant (KOH) consumed for the analyte, mL; C_{KOH} is the exact concentration of the titrant (KOH), mol·L^{-1}; m is the mass of the analyzed sample, g; and M_{KOH} is the KOH molar mass, g·mol^{-1}.

Epoxy Group Content Determination. To about 0.2 g of the sample, 10 mL of 0.2 M HCl in acetone was added. The solution was stirred for 1 h and titrated with a known concentration of 0.1 M KOH solution. The epoxy group content was calculated according to eqs 2 and 3.

$$n_{\text{epoxy,mmol/g}} = (V_{\text{blank}} - V_{\text{analyte}}) \times C_{\text{KOH}}/\text{m} \quad (2)$$

$$\%_{\text{epoxy}} = \frac{n_{\text{epoxy}} \times 15.9994}{10} \quad (3)$$

where n_{epoxy} is the epoxy group amount per sample, mmol × g^{-1}; V_{Blank} is the volume of the titrant (KOH) consumed without the analyte, mL; V_{analyte} is the volume of the titrant (KOH) consumed for the analyte, mL; C_{KOH} is the exact concentration of the titrant (KOH), mol × L^{-1}; m is the mass of the analyzed sample, g; and 15.9994 is the molar mass of oxygen, g × mol^{-1}.

Titration and Degree of Substitution (DS). The acetyl content (%A) was calculated using the eq 4

$$\%A = ((D - C)N_a + (A - B)N_b) \times 4.305/W \quad (4)$$

where C and D are the volumes (mL) of HCl necessary for the titration of the sample and blank, A and B are the volumes (mL) of NaOH solution necessary for the titration of the sample and blank, N_a and N_b are the normalities of NaOH and HCl solutions, and W is the mass of the CNC sample used.[28] Titration was repeated four times to achieve accurate results.

The degree of substitution (DS) was calculated using eq 5, where the value %A was obtained from eq 4.[28]

$$\text{DS} = 162 \times \%A/(4305 - 43 \times \%A) \quad (5)$$

Fourier-Transform Infrared Spectroscopy (FTIR-ATR). A Nicolet 6700 spectrometer (Thermo Scientific, Waltham, Germany) was used at a resolution of 4 cm^{-1} from 400 to 4000 cm^{-1}, where the average of 16 scans was taken and the average spectrum of each sample was corrected with the baseline.

The double bond conversion rate % (DBC%) was calculated using the eq 6

$$\text{DBC\%} = \left(1 - \left(\frac{A_t}{A_{\text{ra}}}\right)/\left(\frac{A_0}{A_{\text{rb}}}\right)\right) \times 100\% \quad (6)$$

where A_{rb} and A_{ra} are the absorption intensities of the peak at 1733 cm^{-1}, which correspond to (C═O) before and after UV-cross-linking; A_0 and A_t are the absorption intensities of the 810 cm^{-1} bond group (C═C) peak before and after UV-cross-linking.[11]

The theoretical FTIR spectra were calculated using eq 7

$$A_{\text{Xf}} = X \times A_{\text{f}} + (1 - X)A_{\text{pol}} \quad (7)$$

where A_{f} and A_{pol} are the absorbances (%) for components in the composition spectra, cellulose nanocrystal component (f), and polymer matrix (p), respectively. X = wt % of a cellulose nanocrystal component in a specific composition.

Nuclear Magnetic Resonance spectroscopy (NMR). ^{1}H and ^{13}C solutions NMR spectra were acquired on a Bruker AVANCE NEO spectrometer operating at 500 MHz ^{1}H frequency using room temperature 5 mm BBO iProbe. To improve the solubility of CNC and its products, urea, thiourea, and NaOD were added to the solutions in D_2O.

^{13}C CP MAS NMR spectra were recorded on Bruker AVANCE-II spectrometer at 14.1 T magnetic field using a home-built double resonance magic-angle-spinning probe for 4 × 25 mm Si_3N_4 rotors. The spinning speed of the sample was set to 12.5 kHz. The spectrum was recorded with an ordinary cross-polarization (CP) pulse sequence, where the duration of the ramped polarization transfer pulse was 2 ms; the CP pulse was followed by the acquisition in the presence of proton decoupling by a strong frequency-modulated rf field in the proton channel. The relaxation delay between the excitations was 5 s. The intensities in the spectra were normalized to the number of accumulations and the weight of the sample.

Atomic Force Microscopy. Atomic force microscopy (AFM) was performed on a Smena NT-MDT (Moscow, Russia) with HA_NC (ETALON) tip in semicontact mode to scan CNC particle size and the 3D-printed sample fracture surface. A nanocellulose water suspension of 0.005 wt % was applied to a substrate (Si glass) and dried overnight at 40 °C. For fracture surface characterization, samples were broken under ambient conditions. The diameter was measured from the height in the topography, with corrections applied to both the diameter and length to account for the apparent dimensions introduced by the tip. An average value from 100 measurements was used for particle size determination.

Scanning Electron Microscopy (SEM). The surface morphology of the nanocomposites was visualized using a Tescan Mira\LMU scanning electron microscope (Czech Republic). The samples were prepared by fracturing in liquid nitrogen. An acceleration voltage of 2 kV was applied for image generation, and magnification was set to 25,400×.

Surface Contact Angle. A Theta Lite optical tensiometer (Beijing, China) was used to test the surface contact angle with water. CNC filler was applied to a glass substrate and dried overnight at 40 °C. The contact angle was determined at the fifth second at 20 °C. The average of five measurements is presented.

Thermogravimetric Analysis (TGA). A Mettler TG50 instrument (Greifensee, Switzerland) was used to determine the nanocellulose and printed sample thermal stability from the weight loss heating curves at a range of 25−750 °C, with a heating rate of 10 °C min^{-1}, under N_2 atmosphere. Approximately 10 mg of samples were used for the measurements.

Optical Microscopy. A Leica 301-371.011 DMRBE optical microscope (Germany) equipped with 20× magnification

https://doi.org/10.1021/acsomega.4c04419
ACS Omega 2024, 9, 42786−42798

objectives and Leica application suite software was used to obtain images of the top and side surfaces of the 3D-printed samples and analyze 3D printing quality.

UV−vis Spectroscopy. A SolidSpec3700 UV−vis-NIR Shimadzu (Kyoto, Japan) spectrophotometer was used to analyze transmittance and reflectance changes regarding added reinforcement in the wavelength range of 240−700 nm in transmittance and reflectance modes. The 500 nm spectral line was chosen to compare the data. Measurements were performed on printed rectangle samples (80 × 10 × 4 mm).

Density Analysis. The hydrostatic weighing was used on a Sartorius MC1 analytical balance (Germany, Burladingen) to determine the density of the printed samples. Samples of approximately 45 mg were prepared, and then 10 parallel measurements in air and ethanol were carried out. The scale accuracy was 0.00001 g.

The sample density was calculated according to eq 8

$$\rho = \frac{m_a \times (\rho_{C_2H_5OH} - 0.0012)}{0.99983 \times (m_a - m_{C_2H_5OH})} + 0.0012 \quad (8)$$

where ρ is the density of the sample, m_a is the mass of the sample in air, $\rho(C_2H_5OH)$ is the density of the used ethanol, and $m(C_2H_5OH)$ is the mass of the sample in ethanol. 0.0012 is the air density value.

Sol Fraction Analysis. A Soxhlet extraction setup was used to determine the part of the polymer that is not cross-linked. Ten parallel samples (4 × 4 × 2 mm) of each printed composition were prepared. Sol fraction analysis was performed in acetone for 72 h.

Spectrophotometer Analysis. The printed samples' color changes regarding reinforcement were evaluated using the Ci7600 Sphere Benchtop Spectrophotometer (x-rite Pantone, Michigan). Three parallel measurements were done with a total transmittance aperture of 6 mm, a wavelength range of 360−750 nm, a photometric resolution of 0.01%, and white paper to avoid color darkening from black background due to the transparency of the samples.

Tensile and Flexure Tests. A universal mechanical testing device from Tinius Olsen (Horsham, PA) was used to test the printed samples in tensile and flexure modes. All printed samples were tested in a constant mode at 1 mm/min modulus at first and 5 mm min^{-1} after. Samples (80 × 10 × 4 mm) were tested 2 days after being printed at room temperature. At least five replicates were used for each sample.

Dynamic Mechanical Analysis (DMA). A Mettler SDTA861e (Columbus, OH) dynamic mechanical analyzer was used to analyze printed samples (80 × 10 × 4 mm) in a temperature range of −70 to 100 °C with a heating rate of 3 °C min^{-1}, a frequency of 1 Hz, and a force of 5 N.

To determine the molecular weight between cross-links, M_c and cross-linking density N were calculated using eqs 9 and 10:

$$M_c = \frac{3\rho RT}{E'} \quad (9)$$

$$N = \frac{\rho}{M_c} \quad (10)$$

where ρ is the density of the printed sample, E' is the storage modulus at 95 °C, T is the temperature at which E' is acquired, and R is the gas constant.

RESULTS AND DISCUSSION

Functionalization of CNCs. The modification of CNC is achieved by the formation of new covalent bonds with long fatty acids using green CNC esterification without any hazardous solvents.[25,27,29] To examine the modification process, the comparison of the FTIR spectra for the neat and functionalized CNC is shown in Figure 2a, and NMR

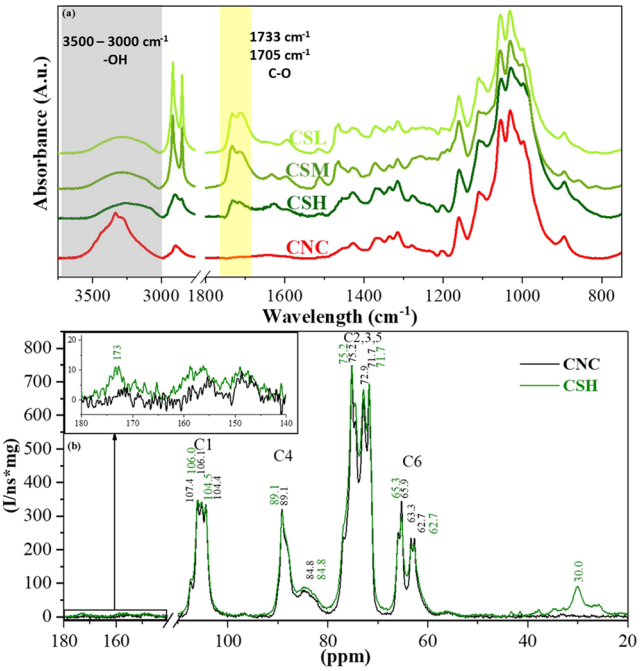

Figure 2. FTIR spectra of CNC and SFA-functionalized CNC (a), and the ^{13}C CP MAS solid-state NMR spectra of CNC and SFA-functionalized CSH (b).

spectra were acquired to validate the observations from the FTIR spectra. Figure 2b shows solid-state ^{13}C NMR spectra of CNC and the functionalized CNC. ^{1}H (Figure S2a,b) and ^{13}C (Figure S2c) spectra for soluble starting materials (SFAs). Figure S3 shows the ^{1}H spectra of SH, CNC, a physical mixture of both, and the functionalized CNC (CSH) of the esterification reaction.

The broad absorption peak between 3500 and 3000 cm^{-1} (FTIR spectra Figure 2a gray area) is attributed to the −OH vibrations for CNC, which is also the location of the esterification reaction.[30] The spectral changes show a notable intensity drop, indicating the successful formation of ester linkages. The structure of each glucopyranose unit contains three hydroxyl groups, which are not isolated but part of a noncovalently linked network of cellulose polymers. These also represent steric challenges and limitations for the surface modification reaction of CNC. The main goal of modification is to reduce the hydrophilicity of the CNC surface and enhance noncovalent linking between matrix and filler. The yellow area in Figure 2a is where the carbonyl groups (from ester) can be observed. Additional spectra containing all six SFAs and all six modification products are provided in the Supporting Information (Figure S1). The peaks at 1733 cm^{-1} belong to the stretching vibrations of esters' carbonyl groups.[11,25] The peak at 1705 cm^{-1} is attributed to the carbonyl group of carboxylic acid.[22] It can be seen that two peaks overlap with SFA's peaks, but the reduction in the

https://doi.org/10.1021/acsomega.4c04419
ACS Omega 2024, 9, 42786−42798

Table 1. Nanocellulose and SFA Parameters

sample	CNC	CSH	CSM	CSL	CSH 1	CSM 1	CSL 1
diameter (nm)	33 ± 2	38 ± 4	34 ± 5	34 ± 5			
length (nm)	259 ± 74	283 ± 76	308 ± 64	276 ± 69			
T_{max} (°C)	360	320	337	357			
char yield (%)	11	20	17	14			
contact angle (deg)	0	62 ± 2	59 ± 1	56 ± 2			
acetyl content		7.88 ± 0.21	6.71 ± 0.15	4.82 ± 0.17	5.25 ± 0.12	6.84 ± 0.2	4.82 ± 0.19
degree of substitution		0.32 ± 0.01	0.27 ± 0.02	0.19 ± 0.018	0.31 ± 0.03	0.27 ± 0.02	0.21 ± 0.03
acid group[a] (mmol g^{-1})		1.80 ± 0.05	1.71 ± 0.02	0.41 ± 0.03	2.17 ± 0.05	1.22 ± 0.01	1.06 ± 0.02
epoxy group[a] (mmol g^{-1})		0.08 ± 0.01	0.30 ± 0.01	0.44 ± 0.02	0.09 ± 0.01	0.21 ± 0.01	0.26 ± 0.01

[a]Attributed to SFA.

original carboxylic acid and an increase in the formed ester's carbonyl group peaks can be observed (see Figure S1). These spectra also depict the appearance of two complete and distinctive peaks of long aliphatic chains of SFA at 2911 and 2850 cm^{-1}, indicating the presence of SFA in CNC samples.

In the solution-state 1H NMR spectra (Figure S3), SH exhibits characteristic signals of fatty acid chains in the spectral region from 1.0 to 2.1 ppm and signals characteristic of hydroxy and epoxy groups containing fragments at ∼3.4 and 3.8 ppm. In the region from ∼6 to ∼7.2 ppm, signals corresponding to double bonds and aromatics-containing fragments can be observed, although in lower amounts than fatty acids. Characteristic signals of the cellulose are observed in the region from ∼3.2 to 4.6 ppm. The most intensive peak (from cellulose) at ∼3.3 ppm corresponds to an overlap of the primary alcohol-containing CH_2−OH group signal and cellulose core signals. In the physical mixture of two components, this peak is at the same position, although its relative intensity appears to be decreased due to the overlap of signals at ∼3.4 ppm. In the spectrum of the synthesized product, we see that the most intensive peak is shifted downfield to ∼3.35 ppm, and the shape of the signal has changed because of the acylation of the alcohol group. However, the degree of substitution at this position cannot be estimated due to overlap. The ^{13}C CP MAS solid-state NMR spectra (Figure 2b) show a comparison of the starting cellulose and the product of esterification with SFA CSH (spectra of CSM and CSL in Figure S4a,b). The intensities in the spectra are normalized to the intensity of the glycosidic carbon in the cellulose structure; thus, we can observe a decrease in the relative intensity of the peaks at ∼63 and 65 ppm, where signals of the CH_2−OH group manifest. At the same time, we can observe a broadened signal at ∼173 ppm, characteristic of carboxylic derivatives such as esters. The peak at ∼30 ppm is characteristic of aliphatic carboxylic acid derivatives in the SFA. Thus, the combination of ^{1}H solution and ^{13}C solid-state spectra corroborates observations from the FTIR spectra that functionalization via carboxylic acid esters has occurred.

Functionalization of CNC was also analyzed by calculating the degree of substitution (DS) according to eq 5.[31] All the DS are summarized in Table 1, showing that higher acid group concentrations in the SFA also ensure higher DS. The modifications yield three distinct modified CNC types based on DS; therefore, the highest (CSH), the lowest (CSL), and the value in the middle (CSM) were selected for further research.

Characterization of the Fillers. CNC dimensions were controlled with AFM measurements (Figure S5). The dimensions of CNC and functionalized CNC particles are summarized in Table 1. AFM measurements determined that the functionalized CNC particles slightly increased in size compared to the CNCs. The size variations are relatively small and can be attributed to measurement errors related to the number of particles measured, orientation, and agglomeration. Surface wetting tests were performed on solvent-cast CNC films (Table 1 and Figure S5) to determine the hydrophobicity of the nanocellulose surface. The contact angle was determined in the fifth second of the measurement. A water droplet was instantly adsorbed on the CNC film's surface, yielding a contact angle (θ) 0°. The SFA-functionalized CNC wetting angle ranged from 56 to 62°. SFA significantly reduced the hydrophilic properties of the CNC surface but did not yield a hydrophobic surface. These results could be attributed to the distinct chemical composition of SFA, steric challenges, and a lack of reaction parameter optimization. It is expected that after long SFA chains attach to the cellulose unit, accessibility to neighboring hydroxyl groups for reaction becomes much more challenging. In comparison, water molecules are relatively small. Still, the wetting measurements show that the CNC functionalization was successful, the contact angle was increased, and the hydrophilic properties of the surface were reduced.

Thermogravimetric analysis was carried out to investigate the thermal stability of functionalized CNC (Figure S6). Table 1 summarizes the maximum degradation temperature (T_{max}) and char yield values. Notable is that both CNC and functionalized CNC show initial degradation at around 280 °C. It is evident that a significant drop in T_{max} occurs when the number of acid groups in SFAs utilized for functionalization increases. This effect could be related to the thermal degradation of the ester bonds formed between the CNC and SFAs, which lead to the formation of carboxyl groups, which can catalyze the degradation process of the CNC. Comparable tendencies for several forms of cellulose and bioderived polymers have been noted in the literature.[32−34] The weight loss curves of SFAs in Figure S6b are indicative of a catalytic impact of carboxyl groups, which show that both the functionalized CNCs and the SFAs themselves degrade more quickly when the acid content of the SFAs increases. However, further research is needed to properly assess the complete spectrum of conversions that take place during the thermal degradation of such intricate systems. The decomposition of suberin components is characteristic at ∼400 °C and around 440−450 °C, which is attributed to the degradation of ω-hydroxy acids and α, ω-diacids, respectively.[35] The lack of these peaks (CSH) or reduced intensity (CSM) is shown in Figure S6a and is a direct indication of a higher degree of

https://doi.org/10.1021/acsomega.4c04419
ACS Omega 2024, 9, 42786−42798

substitution. The char yield of nanocellulose at 700 °C is between 11 and 20%, with the SFA contributing to higher values.

Characterization of the 3D-Printed Samples: Filler and Matrix Interface Synergy. FTIR analysis was applied to investigate the hydrogen bonding and noncovalent bonding between the filler and the polymer matrix at the C═O peak (Figure 3a), while the full spectra of printed samples are shown

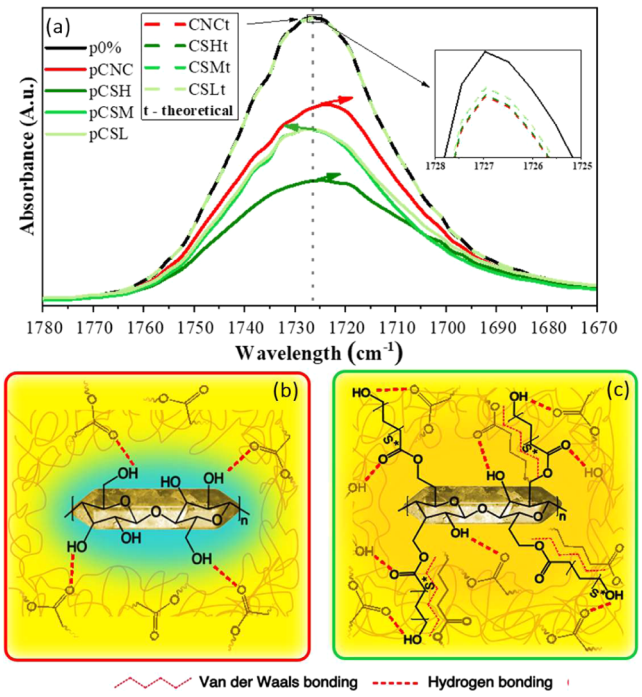

Figure 3. FTIR spectra of the C═O group from the printed sample (a), and schematic representation of proposed filler−matrix interaction for pCNC (b) and pCSH, pCSM, and pCSL (c).

in Figure S8 Previous investigations have shown that the hydrogen bonding effect is visible on the matrix's C═O peak at 1727 cm^{-1}, where intensity drops and the peak shifts.[11,36,37] These changes can be evaluated by calculating the intensity drop associated with the impact of CNC concentration (Lambert−Beer's eq 7), yielding the theoretical FTIR spectra. In contrast, significant deviations from theoretically calculated spectra can be attributed to hydrogen bonding or other types of noncovalent bonding with CNC filler. It has been previously discussed that CNC and AESO-based matrix form a hydrogen bonding.[36,38,39] SFA modification shows a higher impact on the C═O peak than a neat CNC. This could be attributed to strong noncovalent bonding enabled by SFA modifications. Thus, an enhanced interface between filler and matrix is formed, and the formation of hydrogen bonds is promoted. Neat CNC's highly hydrophilic surface usually shows a high affinity for internal linking with itself. The schematic representation of formed hydrogen bonds and noncovalent bonds between matrix and CNC and SFA functionalized CNC is shown in Figure 3b,c, respectively.

Morphology and Print Quality. To evaluate morphology, optical microscopy (top and side surfaces), AFM (fracture surface), and colorimetry were used on 3D-printed rectangle samples. Figure 4a,b show excellent printing accuracy by clearly showing each separate pixel (50 × 50 μm) on rectangle top and side surfaces, respectively. A slight decrease in surface quality can be observed with the added CNC reinforcement. Sample pCSH shows the closest surface quality (both top and side) to the p0% sample with the fewest defects. Figure 4c shows the images of the color changes after adding CNC reinforcement and the color difference factor (ΔE^*_{ab}), which shows the color deviation from the p0%. The most noticeable color change occurs for the pCSH sample (ΔE^*_{ab} = 5.7) and the least for the pCSM sample (ΔE^*_{ab} = 3.1). Still, the ΔE^*_{ab} value changes are relatively small, i.e., the difference is noticeable by an experienced observer if ΔE^*_{ab} < 2; between 3.5 and 5, the difference is noticeable; ΔE^*_{ab} > 5, there is an impression of two different colors.[40] While other sources state that ΔE^*_{ab} values between 3 and 6 are usually considered acceptable in commercial reproduction, printing, and graphic professionals may perceive the color difference.[41]

AFM measurements were performed on a cross-section fracture surface in semicontact mode, and 3D images of the surface are shown in Figure 4d. The calculated surface roughness (Rq (RMS)) is p0% = 14.2 ± 3.9, pCNC = 8.3 ± 1.5, and pCSH = 10.7 ± 2.6 nm. The results show no significant difference. At the same time, the visual changes show a slightly rougher surface texture for pCNC and pCSH. This leads to the main observation that CNC integration into the matrix resulted in good filler dispersion. UV−vis spectroscopy measurements (Figure S7) determined the light transmittance, reflectance, and absorbance at 500 nm; the values obtained are shown in Table 2. Adding a neat CNC to the polymer matrix did not change the transparency. Meanwhile, SFA functionalized CNC addition resulted in decreased transparency. This could be related to the structural changes and enhanced noncovalent bonding or suberin extraction byproducts retained on the surface of CNC. Figure 4e shows the fracture surfaces of nanocomposites. All CNCs appear to be well dispersed without any visible agglomeration.

Macromolecular Chain Network Formation and Stability. Photo-cross-linked acrylate performance depends on the formed polymer network. Selected parameters−the double bond conversion rates (DBC%), density, sol fraction, molecular weight between cross-links (M_c), and cross-link density (N) − were chosen to characterize this process. Measured and calculated values are summarized in Table 2. The FTIR spectra of resins and cured samples from which DBC% was calculated with eq 6 are shown in Figure S8. The mechanical properties and stiffness of the obtained materials are significantly dependent on the conversion of functional groups.[42] Table 2 shows that the highest DBC% is for the p0% sample (83%), where no filler restricts radical and molecular movements, and hence, a higher DBC% can be achieved. Filler-reinforced samples show a drop of DBC% around 10%, with the notable exception of CSH showing only half of that. Correlation is observed with sol fraction data, with the lowest sol fraction being 3.7 ± 0.2% for p0% and 5.0−6.8% for filler-reinforced samples.

Further insights about the macromolecular chain network and filler interaction with the matrix are analyzed with N and M_c calculated by applying the theory of entropic rubber elasticity to the rubbery plateau modulus derived from the DMA measurements.[43,44] This indicates covalent and hydrogen bonding and all types of cross-links active in the system (chemical and physical). pCSH shows the highest value of N, indicating that the sum of covalent and noncovalent bonding is the highest of all samples. With a 21% reduction, the pCSM sample follows, while the lowest N value is observed for the

https://doi.org/10.1021/acsomega.4c04419
ACS Omega 2024, 9, 42786−42798

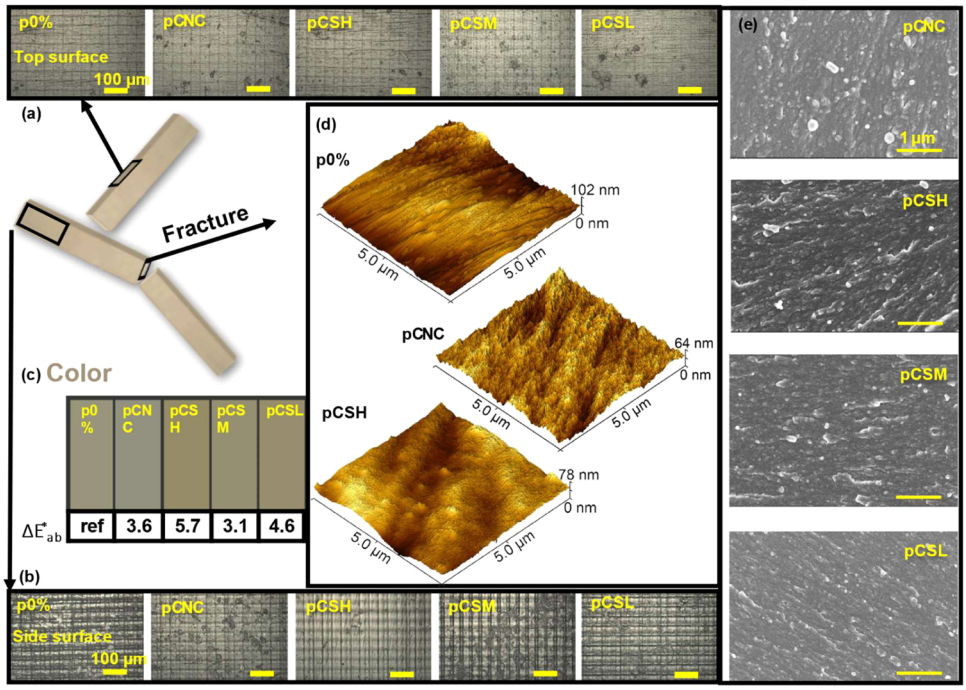

Figure 4. Printed rectangle sample optical microscopy images of the top (a) and side (b) surfaces, colorimetry images with color deviation ΔE^*_{ab} (c), AFM 3D images of fracture surface (d), and SEM images of fracture surface (e).

Table 2. Characteristics of the 3D-Printed Samples

3D-printed samples	p0%	pCNC	pCSH	pCSM	pCSL
DBC%, (%)	83	72	78	71	73
sol fraction, (%)	3.7 ± 0.2	5.6 ± 0.8	5.0 ± 0.6	6.1 ± 0.7	6.8 ± 0.7
N, (mmol/cm)^3	1.1	1.8	3.3	2.6	2
M_c, (g/mol)	1021	600	336	421	563
density, (g/cm^3)	1.128 ± 0.001	1.125 ± 0.002	1.112 ± 0.005	1.116 ± 0.001	1.119 ± 0.002
T_{max}, (°C)	423	418	421	416	420
char yield, (%)	3	4	4	2	3
T_{g1}, (°C)	46	72	66	65	66
T_{g2}, (°C)		80	72	73	70
transmittance at 500 nm, (%)	78	78	68	72	68
reflectance at 500 nm, (%)	7	7	6	7	7
absorbance at 500 nm, (%)	15	15	26	21	25

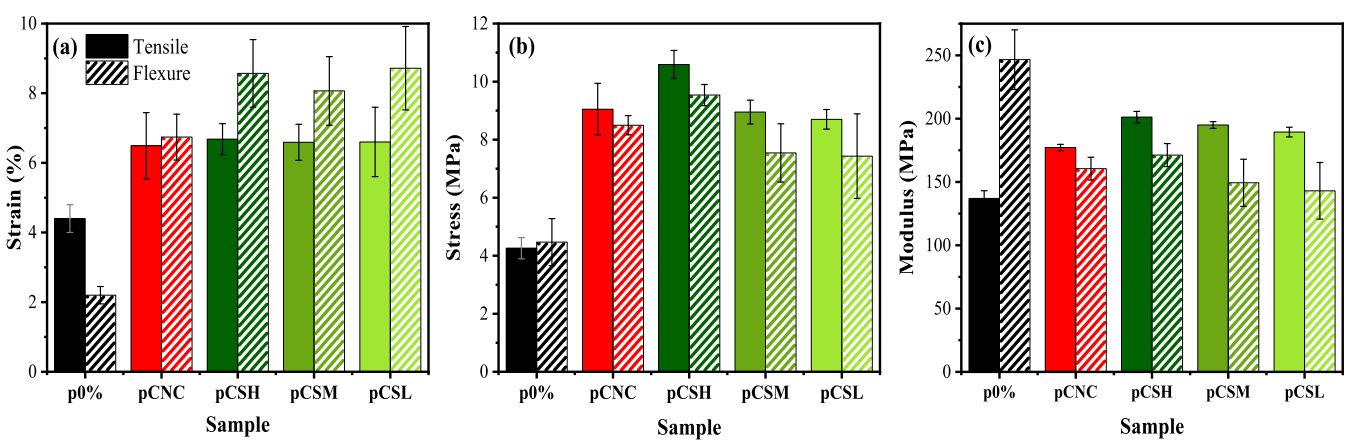

Figure 5. Tensile and flexural properties of the 3D-printed samples—strain (a), stress (b), and modulus (c).

p0% sample. Matching observation is presented by M_c, with the highest molecular weight between cross-link for the p0% and the lowest for pCSH.

TGA measurements were also used to evaluate the thermal stability of the 3D-printed nanocomposite samples. The weight loss and derivative weight curves can be seen in Figure S9.

https://doi.org/10.1021/acsomega.4c04419
ACS Omega 2024, 9, 42786−42798

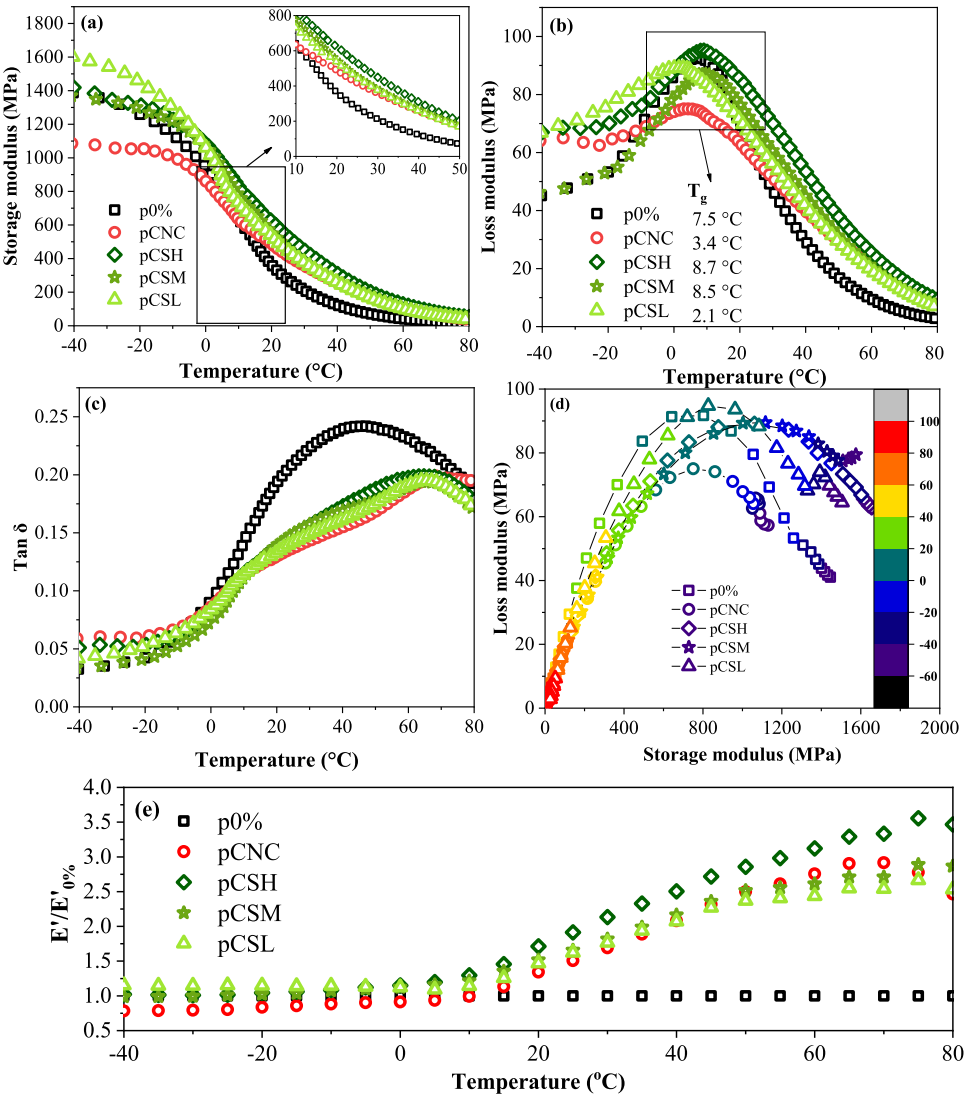

Figure 6. Storage modulus (a), loss modulus (b), tan δ (c), Cole−Cole plot (d) of the 3D-printed samples, and the ratio between storage modulus of p0% and CNC-reinforced composites (e).

According to the peak values, the maximum weight loss is observed at around 420 °C. The polymer matrix offers thermal protection to the functionalized CNC.[14] The main peak can be attributed to the degradation of the AESO polymer matrix.[45] No significant deterioration of thermal stability can be observed with the addition of functionalized CNC fillers. This is mainly due to the low content of the introduced nanocellulose. The main degradation temperature ranges from 418 to 423 °C, the highest for the p0% sample (T_{max} = 423 °C). With added fillers, the nanocomposite samples showed a decrease in T_{max} by 2−5 °C. The primary weight loss occurs in the range of 290−500 °C. Depending on which type of SFA-functionalized CNC is used, the first 5 wt % are lost at 327−337 °C. Char yield (%) for all printed samples is very similar, between 2 and 4%.

Mechanical Properties of 3D-Printed Samples. The mechanical performance of composites defines their limits in future applications. Notably, Figure 5 demonstrates that introducing nanocellulose significantly increased mechanical strength and failure strain for the 3D-printed composites. Among all the composites examined, the emphasis on suberin-functionalized composites reveals equivalent or superior performance to their petroleum-functionalized counterparts described in the literature.[11,46] The primary focus should be on comparing the performance of neat versus functionalized fillers. In our previous research, our group conclusively demonstrated the advantages of incorporating nanocellulose into the vegetable oil−acrylate matrix.[11,38] Such analysis framing will help to understand the value added from SFA functionalization.

Figure 5a shows that the maximal strain achieved for the tensile test is almost identical for all the composites, with a small increase for the pCSH composite, although within the error margins of other composites. For composites, the increase for maximal strain is around 60% compared with a neat p0% sample. The result variance (error margin) decreases with the increased degree of hydroxyl group substitution in modified CNC. This observation implies that the higher functionalization efficiency helps to achieve higher replicability in the samples (same for stress and modulus results). This effect is achieved due to improved compatibility between the matrix and CSH compared to other fillers. The lack of functionalization or its' decreased efficiency leads to reduced van der Waals bonds being formed.

https://doi.org/10.1021/acsomega.4c04419
ACS Omega 2024, 9, 42786−42798

On the contrary, the flexural tests show a substantial 30.7% increase in maximal strain for the pCSH composite compared to the pCNC. Such a difference in results is easily explained by the nature of the deformation in both tests. The tensile loading influences the whole specimen simultaneously, while in the flexural tests, only half of the sample is influenced,[47] meaning fewer defects are involved. For a tensile test, the weakest failure point mainly determines the performance of the sample, while in a flexural test, the number of weakest points is the limiting factor. Considering this, it is evident that the SFA functionalization helps reduce the number of "weakest points" through improved compatibility. In terms of maximal stress (Figure 5b), the pCNC, pCSM, and pCSL achieved similar results within the error margin; however, the pCSH achieved a 14.5 and 85.7% increase in comparison to the pCNC and p0%, respectively. The modulus values (Figure 5c) follow the preceding trend. Compared to pCNC, the SFA-functionalized CNC composites achieved higher modulus values, with up to 11.1% higher values for tensile tests and 6% higher for flexural tests.

Our primary hypothesis posits that the distribution of the filler among the layers and the specific properties of the filler, particularly the length-to-diameter ratio, are critical determinants of the mechanical properties observed. During the printing process, the filler is uniformly dispersed within each layer; however, it does not facilitate strong interlayer connections. Consequently, during tensile testing, each individual layer, reinforced with nanofillers, contributes to the overall mechanical performance of the 3D-printed samples, resulting in enhanced strength and modulus. The observed decrease in flexural modulus, accompanied by an increase in strain, suggests that functionalization induces a slight plasticizing effect.

Thermomechanical Characteristics of 3D-Printed Samples and Reinforcement Efficiency. Like all polymers, vegetable oil-based matrixes exhibit strong mechanical property dependence on temperature. The characteristic transition from a glassy to a viscoelastic state is marked by a sharp drop in the sample storage modulus (Figure 6a). With enhanced segmental mobility and molecular relaxation processes in the viscoelastic state, the filler (CNC) can start acting as a matrix reinforcement. The visible differences in the glassy state can be explained by the polymer chain packing and initial compatibility between filler and matrix, as well as the preparation procedure. Thus, pCNC having lower properties than p0% in the glassy state can be attributed to the hydrophobic surface of CNC disrupting the matrix structure; e.g., some extra structural defects could be introduced. These defects are then reduced with segmental mobility achieved during the glass transition. The glass transition temperature (T_g in Figure 6b), obtained from the loss peak maximum, can be used as an initial filler and matrix compatibility marker. Notably, three distinct cases of glass transition temperature can be seen, with pCNC and pCSL having lower values than the reference p0%, while pCSM and pCSH show higher values. A higher glass transition temperature would indicate strong intermolecular bonding between filler and matrix, working to restrict polymer chain mobility. Still, looking at the whole peak together and not just the maximum, the phase transition is notably affected by CNC and SFA-functionalized CNC, as the whole peak was shifted to higher temperatures for all reinforced samples.

Figure 6c shows tan δ curves, representing the ratio between the elastic and viscous responses in the material structure. An apparent peak transformation from a single broad peak (p0%) occurs to form a peak with a large shoulder for all printed samples with CNC. The reduced peak height indicates increased stiffness and rigidity (material behavior shifts toward being more elastic). This matches well with the storage modulus graphs, showing a well-visible difference between p0% and CNC-reinforced samples within a temperature range of 10 to 40 °C. Figure 6d shows the Cole−Cole plot representing the relaxation process changes with the modification of the printed system. pCSM and pCSH show a significant depression of the semicircle (elliptical path), indicating a deviation from the single relaxation time of the ideal semicircle.[48] In other words, the system has two phases. None of the printed samples follow the ideal semicircle shape, which can be attributed to the complexity of the material structure and the random nature of photo-cross-links. The preservation of the Cole−Cole plot's distinct shape also serves as an indicator for good adhesion between filler and matrix. This matches well with the proposed enhanced interface discussed in previous sections. Lastly, Figure 6e shows the storage modulus ratio between neat and reinforced samples. This allows us to identify the temperature region where the reinforcement is effective. Load transfer starts at around 10 °C, and the most significant difference between p0% and CNC-reinforced systems is visible at around 70 °C, reaching a 3.5-fold increase for pCSH. In addition, the difference between pCNC and p0% drops after 70 °C, while SFA-functionalized composites retain reinforcement at a similar level.

CONCLUSIONS

Our aim was to enhance the reinforcement of DLP 3D-printed biobased composites by improving the interface with a novel green functionalization of cellulose nanocrystals (CNC) with suberin fatty acids (SFA). Contact angle measurements indicate successful CNC filler functionalization, evidenced by reduced hydrophilicity, while FTIR and NMR measurements support the successful functionalization via the formation of covalent bonds. As the filler loading in composites was only 0.1 wt % of the total formulation, the thermal stability of the 3D-printed samples remained unaltered. Finally, mechanical analysis revealed improved performance upon adding SFA-functionalized CNC filler to the polymer matrix, enhancing the filler−matrix interface. Tensile measurements showed significant enhancements in elasticity, strength, and strain modulus. Notably, the highest mechanical properties were observed for pCSH, attributed to its higher degree of hydroxyl group substitution. Thermomechanical analysis revealed higher compatibility between matrix and SFA-modified CNC. There are several routes to continue the research. First, focus on improving the mechanical performance of neat AESO resin and the search for alternative biobased monomers; which, combined with functionalized fillers, will allow us to overcome the petroleum-based resins. Second, focus on biorefinery processes from the wood factory waste and enhance the extraction procedures to further incorporate circular economy approaches and sustainable chemistry.

ASSOCIATED CONTENT

Supporting Information

The Supporting Information is available free of charge at https://pubs.acs.org/doi/10.1021/acsomega.4c04419.

https://doi.org/10.1021/acsomega.4c04419
ACS Omega 2024, 9, 42786−42798

Suberin fatty acid extraction conditions. GC-MS analysis of the SFA samples. (Tables S1−S9). FTIR spectra for all suberin fatty acids and functionalized CNC; NMR spectra of SFA variations and functionalized CNC; AFM and surface contact angle images; TGA/DTG curves for CNC fillers; UV−vis spectra of 3D-printed samples; FTIR spectra of resins and printed samples; TGA/DTG curves for 3D-printed samples. (Figures S1−S9) (PDF)

AUTHOR INFORMATION

Corresponding Author

Sergejs Gaidukovs − *Institute of Chemistry and Chemical Technology, Faculty of Natural Sciences and Technology, Riga Technical University, LV-1048 Riga, Latvia;* orcid.org/0000-0001-8638-5009; Email: Sergejs.Gaidukovs@rtu.lv

Authors

Beate Beatrise Bruvere − *Institute of Chemistry and Chemical Technology, Faculty of Natural Sciences and Technology, Riga Technical University, LV-1048 Riga, Latvia;* orcid.org/0009-0003-0767-2416

Anda Gromova − *Institute of Chemistry and Chemical Technology, Faculty of Natural Sciences and Technology, Riga Technical University, LV-1048 Riga, Latvia;* orcid.org/0000-0002-8492-0095

Maksims Jurinovs − *Institute of Chemistry and Chemical Technology, Faculty of Natural Sciences and Technology, Riga Technical University, LV-1048 Riga, Latvia;* orcid.org/0000-0003-4900-2798

Oskars Platnieks − *Institute of Chemistry and Chemical Technology, Faculty of Natural Sciences and Technology, Riga Technical University, LV-1048 Riga, Latvia;* orcid.org/0000-0001-5529-0912

Jānis Rižikovs − *Biorefinery Laboratory, Latvian State Institute of Wood Chemistry, LV-1006 Riga, Latvia;* orcid.org/0000-0002-4825-3053

Aigars Pāže − *Biorefinery Laboratory, Latvian State Institute of Wood Chemistry, LV-1006 Riga, Latvia*

Daniela Godiņa − *Biorefinery Laboratory, Latvian State Institute of Wood Chemistry, LV-1006 Riga, Latvia*

Inese Mieriņa − *Institute of Chemistry and Chemical Technology, Faculty of Natural Sciences and Technology, Riga Technical University, LV-1048 Riga, Latvia*

Ivo Heinmaa − *Naional Institute of Chemical Physics and Biophysics, 12618 Tallinn, Estonia*

Krisjanis Smits − *Baltic Biomaterials Centre of Excellence, Headquarters at Riga Technical University, LV-1048 Riga, Latvia; Institute of Biomaterials and Bioengineering, Faculty of Natural Sciences and Technology, Riga Technical University, LV-1048 Riga, Latvia*

Vitālijs Rjabovs − *Institute of Chemistry and Chemical Technology, Faculty of Natural Sciences and Technology, Riga Technical University, LV-1048 Riga, Latvia*

Complete contact information is available at: https://pubs.acs.org/10.1021/acsomega.4c04419

Author Contributions

S.G. conceived the idea of this study, assembled the team, provided resources, supervised the research, analysis, **B.B.B.** CNC functionalization, resin preparation, printing, FTIR, contact angle, and acid group content measurements, preparation of the initial draft, data curation, visualization, analysis, **A.G.** conceived the idea of this study, CNC functionalization, FTIR and colorimetry analysis, AFM measurements, **M.J.** CNC preparation, TGA and tensile measurements, printing quality supervisor, analysis, visualization, **O.P.** DMA measurements, analysis, preparation of the initial draft, review, editing, **J.R.** SFA extraction supervision and analysis, **A.P.** and **D.G.** SFA extraction, validation, and characterization, **I.M.** liquid NMR measurements and initial analysis, **I.H.** solid NMR measurements and initial analysis, **K.S.** SEM structure investigation, **V.R.** NMR measurement supervision and full NMR analysis. All authors read the final version, discussed the results, and commented on the manuscript.

Funding

B.B.B. research was funded by the Riga Technical University project RTU Nr. ZM-2024/8 for strengthening scientific personnel capacity in 2024. A.G. research was funded by Riga Technical University's Doctoral Grant program.

Notes

The authors declare no competing financial interest.

ACKNOWLEDGMENTS

A.G. acknowledges L'ORÉAL-UNESCO "For Women in Science" Young Talents Program - Baltic with the support of the Latvian National Commission for UNESCO and the Latvian Academy of Sciences. The authors wish to thank their parental institute for providing the necessary facilities to accomplish this work. The authors acknowledge the access to infrastructure and expertise of the BBCE- Baltic Biomaterial Centre of Excellence (European Union's Horizon 2020 research and innovation programme under the grant agreement No. 857287)

REFERENCES

(1) Moshood, T. D.; Nawanir, G.; Mahmud, F.; Mohamad, F.; Ahmad, M. H.; AbdulGhani, A. Sustainability of biodegradable plastics: New problem or solution to solve the global plastic pollution? *Curr. Res. Green Sustainable Chem.* **2022**, *5*, No. 100273.

(2) Shuaib, M.; Haleem, A.; Kumar, S.; Javaid, M. Impact of 3D Printing on the environment: A literature-based study. *Sustain. Oper. Comput.* **2021**, *2*, 57−63.

(3) Sutton, J. T.; Rajan, K.; Harper, D. P.; Chmely, S. C. Lignin-Containing Photoactive Resins for 3D Printing by Stereolithography. *ACS Appl. Mater. Interfaces* **2018**, *10* (42), 36456−36463.

(4) Nurchi, C.; Buonvino, S.; Arciero, I.; Melino, S. Sustainable Vegetable Oil-Based Biomaterials: Synthesis and Biomedical Applications. *Int. J. Mol. Sci.* **2023**, *24* (3), 2153.

(5) Robles, E.; Urruzola, I.; Labidi, J.; Serrano, L. Surface-modified nano-cellulose as reinforcement in poly(lactic acid) to conform new composites. *Ind. Crops Prod.* **2015**, *71*, 44−53.

(6) Klemm, D.; Heublein, B.; Fink, H. P.; Bohn, A. Cellulose: fascinating biopolymer and sustainable raw material. *Angew. Chem., Int. Ed.* **2005**, *44* (22), 3358−3393.

(7) Bangar, S. P.; Harussani, M. M.; Ilyas, R. A.; Ashogbon, A. O.; Singh, A.; Trif, M.; Jafari, S. M. Surface modifications of cellulose nanocrystals: Processes, properties, and applications. *Food Hydrocolloids* **2022**, *130*, No. 107689.

(8) Feng, X.; Yang, Z.; Chmely, S.; Wang, Q.; Wang, S.; Xie, Y. Lignin-coated cellulose nanocrystal filled methacrylate composites prepared via 3D stereolithography printing: Mechanical reinforcement and thermal stabilization. *Carbohydr. Polym.* **2017**, *169*, 272−281.

(9) Anžlovar, A.; Huskić, M.; Žagar, E. Modification of nanocrystalline cellulose for application as a reinforcing nanofiller in PMMA composites. *Cellulose* **2016**, *23* (1), 505−518.

(10) Feng, X.; Wu, Z.; Xie, Y.; Wang, S. Reinforcing 3D Print Methacrylate Resin/Cellulose Nanocrystal Composites: Effect of Cellulose Nanocrystal Modification. *Bioresources* **2019**, *14* (2), 3701−3716.
(11) Jurinovs, M.; Barkane, A.; Platnieks, O.; Beluns, S.; Grase, L.; Dieden, R.; Staropoli, M.; Schmidt, D. F.; Gaidukovs, S. Vat Photopolymerization of Nanocellulose-Reinforced Vegetable Oil-Based Resins: Synergy in Morphology and Functionalization. *ACS Appl. Polym. Mater.* **2023**, *5* (4), 3104−3118.
(12) Qian, Y. Q.; Han, N.; Bo, Y. W.; Tan, L. L.; Zhang, L. F.; Zhang, X. X. Homogeneous synthesis of cellulose acrylate-g-poly (n-alkyl acrylate) solid-solid phase change materials via free radical polymerization. *Carbohydr. Polym.* **2018**, *193*, 129−136.
(13) Tang, J.; Sisler, J.; Grishkewich, N.; Tam, K. C. Functionalization of cellulose nanocrystals for advanced applications. *J. Colloid Interface Sci.* **2017**, *494*, 397−409.
(14) Ferreira, F. V.; Pinheiro, I. F.; Gouveia, R. F.; Thim, G. P.; Lona, L. M. F. Functionalized cellulose nanocrystals as reinforcement in biodegradable polymer nanocomposites. *Polym. Compos.* **2017**, *39*, E9−E29, DOI: 10.1002/pc.24583.
(15) Correia, V. G.; Bento, A.; Pais, J.; Rodrigues, R.; Halinski, L. P.; Frydrych, M.; Greenhalgh, A.; Stepnowski, P.; Vollrath, F.; King, A. W. T.; Silva Pereira, C. The molecular structure and multifunctionality of the cryptic plant polymer suberin. *Mater. Today Bio* **2020**, *5*, No. 100039.
(16) Tupciauskas, R.; Rizhikovs, J.; Grinins, J.; Paze, A.; Andzs, M.; Brazdausks, P.; Puke, M.; Plavniece, A. Investigation of suberinic acids-bonded particleboard. *Eur. Polym. J.* **2019**, *113*, 176−182.
(17) Handiso, B.; Valle-Delgado, J. J.; Johansson, L.-S.; Hughes, M. The physicochemical properties of cellulose surfaces modified with (depolymerised) suberin and suberin fatty acid. *Ind. Crops Prod.* **2021**, *159*, No. 113070, DOI: 10.1016/j.indcrop.2020.113070.
(18) De Oliveira, H.; Yoon, B.; Michaud, V.; Nam, J.-D.; Suhr, J. All natural cork composites with suberin-based polyester and lignocellulosic residue. *Ind. Crops Prod.* **2017**, *109*, 843−849.
(19) Ferreira, R.; Garcia, H.; Sousa, A. F.; Freire, C. S. R.; Silvestre, A. J. D.; Rebelo, L. P. N.; Silva Pereira, C. Isolation of suberin from birch outer bark and cork using ionic liquids: A new source of macromonomers. *Ind. Crops Prod.* **2013**, *44*, 520−527.
(20) Miranda, I.; Gominho, J.; Mirra, I.; Pereira, H. Fractioning and chemical characterization of barks of Betula pendula and Eucalyptus globulus. *Ind. Crops Prod.* **2013**, *41*, 299−305.
(21) Pinto, P. C.; Sousa, A.; Silvestre, A.; Neto, C.; Gandini, A.; Eckerman, C.; Holmbom, B. Quercus suber and Betula pendula outer barks as renewable sources of oleochemicals: A comparative study. *Ind. Crops Prod.* **2009**, *29*, 126−132.
(22) Rizhikovs, J.; Brazdausks, P.; Paze, A.; Tupciauskas, R.; Grinins, J.; Puke, M.; Plavniece, A.; Andzs, M.; Godina, D.; Makars, R. Characterization of suberinic acids from birch outer bark as bio-based adhesive in wood composites. *Int. J. Adhes. Adhes.* **2022**, *112*, No. 102989.
(23) Qasim, U.; Sirviö, J. A.; Suopajärvi, T.; Hu, L.; Pratiwi, F. W.; Lin, M. K. T. H.; Anghelescu-Hakala, A.; Ronkainen, V.-P.; Xu, C.; Liimatainen, H. A multifunctional biogenic films and coatings from synergistic aqueous dispersion of wood-derived suberin and cellulose nanofibers. *Carbohydr. Polym.* **2024**, *338*, No. 122218.
(24) Shulga, G.; Rizhikovs, J.; Neiberte, B.; Verovkins, A.; Vitolina, S.; Betkers, T.; Makars, R. Processing and Properties of Wood-Plastic Composite Containing Alkali-Treated Birch Wood Shavings and Bioadditive Obtained by Biorefinery of Birch Bark. *Forests* **2023**, *14* (9), 1906.
(25) Lu, J.; Lang, J.; Lan, P.; Yang, H.; Yang, J.; Wu, X.; Zhang, H. Evalution of surface activity of hydrophobic modified nanocrystalline cellulose. *Cellulose* **2020**, *27* (16), 9299−9309.
(26) Godiņa, D.; Paze, A.; Rizhikovs, J.; Stankus, K.; Virsis, I.; Nakurte, I. Stability Studies of Bioactive Compounds from Birch Outer Bark Ethanolic Extracts. *Key Eng. Mater.* **2018**, *762*, 152−157.
(27) Wang, X.; Wang, N.; Xu, B.; Wang, Y.; Lang, J.; Lu, J.; Chen, G.; Zhang, H. Comparative Study on Different Modified Preparation Methods of Cellulose Nanocrystalline. *Polymers* **2021**, *13*, 3147.
(28) Fei, P.; Liao, L.; Cheng, B.; Song, J. Quantitative analysis of cellulose acetate with a high degree of substitution by FTIR and its application. *Anal. Methods* **2017**, *9*, 6194−6201.
(29) Zhang, H.; Yang, H.; Lu, J.; Lang, J.; Gao, H. Study on Stability and Stability Mechanism of Styrene-Acrylic Emulsion Prepared Using Nanocellulose Modified with Long-Chain Fatty Acids. *Polymers* **2019**, *11*, 1131.
(30) Atykyan, N.; Revin, V.; Shutova, V. Raman and FT-IR Spectroscopy investigation the cellulose structural differences from bacteria Gluconacetobacter sucrofermentans during the different regimes of cultivation on a molasses media. *AMB Express* **2020**, *10*, No. 84.
(31) Auclair, N.; Kaboorani, A.; Riedl, B.; Landry, V. Effects of surface modification of cellulose nanocrystals (CNCs) on curing behavior, optical, and thermal properties of soybean oil bio-nanocomposite. *J. Coat. Technol. Res.* **2020**, *17* (1), 57−67.
(32) Chrysafi, I.; Ainali, N. M.; Bikiaris, D. N. Thermal Degradation Mechanism and Decomposition Kinetic Studies of Poly(Lactic Acid) and Its Copolymers with Poly(Hexylene Succinate). *Polymers* **2021**, *13* (9), 1365.
(33) Lease, J.; Kawano, T.; Andou, Y. Esterification of Cellulose with Long Fatty Acid Chain through Mechanochemical Method. *Polymers* **2021**, *13* (24), 4397.
(34) Zhao, X.; Anwar, I.; Zhang, X.; Pellicciotti, A.; Storts, S.; Nagib, D. A.; Vodovotz, Y. Thermal and Barrier Characterizations of Cellulose Esters with Variable Side-Chain Lengths and Their Effect on PHBV and PLA Bioplastic Film Properties. *ACS Omega* **2021**, *6* (38), 24700−24708.
(35) Makars, R.; Rizikovs, J.; Godina, D.; Paze, A.; Merijs-Meri, R. Utilization of Suberinic Acids Containing Residue as an Adhesive for Particle Boards. *Polymers* **2022**, *14* (11), 2304.
(36) Barkane, A.; Platnieks, O.; Grase, L.; Gaidukovs, S. Simultaneous wettability and stiffness control of UV-curing vegetable oil resin composites by lignocellulosic components. *Polymer* **2022**, *255*, No. 125154.
(37) Ryu, I. S.; Liu, X.; Jin, Y.; Sun, J.; Lee, Y. J. Stoichiometric analysis of competing intermolecular hydrogen bonds using infrared spectroscopy. *RSC Adv.* **2018**, *8* (42), 23481−23488.
(38) Barkane, A.; Jurinovs, M.; Briede, S.; Platnieks, O.; Onufrijevs, P.; Zelca, Z.; Gaidukovs, S. Biobased Resin for Sustainable Stereolithography: 3D Printed Vegetable Oil Acrylate Reinforced with Ultra-Low Content of Nanocellulose for Fossil Resin Substitution. *3D Print. Addit. Manuf.* **2023**, *10* (6), 1272−1286.
(39) Liu, W.; Fei, Me.; Ban, Y.; Jia, A.; Qiu, R. Preparation and evaluation of green composites from microcrystalline cellulose and a soybean-oil derivative. *Polymers* **2017**, *9*, 541−554.
(40) Mokrzycki, W.; Tatol, M. Color difference Delta E-A survey. *Mach. Graphics Vision* **2011**, *20* (4), 383−411.
(41) ViewSonic. Delta E Color Accuracy. https://www.viewsonic.com/colorpro/articles/detail/deltae2color-accuracy_3 (accessed Nov 14, 2023).
(42) Štaffová, M.; Ondreáš, F.; Svatík, J.; Zbončák, M.; Jančář, J.; Lepcio, P. 3D printing and post-curing optimization of photo-polymerized structures: Basic concepts and effective tools for improved thermomechanical properties. *Polym. Test.* **2022**, *108*, No. 107499.
(43) Kong, D.; Meng, Y.; McKenna, G. B. Determination of the molecular weight between cross-links for different ambers: Viscoelastic measurements of the rubbery plateau*. *Polym. Eng. Sci.* **2022**, *62* (4), 1023−1040.
(44) Pelletier, H.; Belgacem, N.; Gandini, A. Acrylated vegetable oils as photocrosslinkable materials. *J. Appl. Polym. Sci.* **2006**, *99* (6), 3218−3221.
(45) Barkane, A.; Platnieks, O.; Jurinovs, M.; Gaidukovs, S. Thermal stability of UV-cured vegetable oil epoxidized acrylate-based polymer

https://doi.org/10.1021/acsomega.4c04419
ACS Omega 2024, 9, 42786−42798

system for 3D printing application. *Polym. Degrad. Stab.* **2020**, *181*, No. 109347.
(46) Liu, Z.; Knetzer, D. A.; Wang, J.; Chu, F.; Lu, C.; Calvert, P. D. 3D printing acrylated epoxidized soybean oil reinforced with functionalized cellulose by UV curing. *J. Appl. Polym. Sci.* **2022**, *139* (4), No. 51561.
(47) Leguillon, D.; Martin, É.; Lafarie-Frenot, M.-C. Flexural vs. tensile strength in brittle materials. *C. R. Mec.* **2015**, *343* (4), 275−281.
(48) Jyoti, J.; Singh, B. P.; Arya, A. K.; Dhakate, S. R. Dynamic mechanical properties of multiwall carbon nanotube reinforced ABS composites and their correlation with entanglement density, adhesion, reinforcement and C factor. *RSC Adv.* **2016**, *6* (5), 3997−4006.

https://doi.org/10.1021/acsomega.4c04419
ACS Omega 2024, 9, 42786−42798